

Synthesis, Characterization, Visible Light Photocatalytic and Electrical Properties of Zr-doped CeO₂ Nanoparticles

Suresha Erachikkaiah¹, Swamy Sreenivasa^{1*}, Lalithamba Haraluru Shankaraiah², Rashmi³

¹ Department of Studies And Research in Chemistry, Tumkur University, Tumakuru 572 103, Karnataka, India; sureshabig@gmail.com (S.E.);

² Department of Chemistry, Siddaganga Institute of Technology, B.H. Road, Tumakuru-572 103, Karnataka, India; hsl@sit.ac.in;

³ Department of Electrical and Electronics Engineering, Siddaganga Institute of Technology, B.H. Road Tumakuru-572 103, Karnataka, India; rash_mysore@sit.ac.in;

* Correspondence: dr.tumkuruniversity@gmail.com;

Received: 10.02.2025; Accepted: 15.05.2025; Published: 4.09.2025

Abstract: Zirconium-doped cerium oxide nanoparticle of composition Zr_{0.075}-Ce_{0.925}O₂ was prepared by the solution combustion process, and its morphological features were evaluated by FT-IR, SEM, EDX, XRD, and UV-DRS studies. From UV-DRS studies, the band gap of the prepared nanoparticle was determined to be 2.9 eV. Also, the photocatalytic activity of Zr_{0.075}-Ce_{0.925}O₂ nanoparticle was examined for methylene blue dye and found to be an efficient source for the degradation of dye molecules in the visible region. Furthermore, this nanoparticle was inspected for its electrical behaviors and could be applied to sophisticated energy storage systems like thin film capacitors. High dielectric constant and low dissipation factor are demonstrated in this study and give a new insight towards environmental protection.

Keywords: zirconium; cerium oxide; photocatalytic degradation; dielectric constant; storage devices.

© 2025 by the authors. This article is an open-access article distributed under the terms and conditions of the Creative Commons Attribution (CC BY) license (<https://creativecommons.org/licenses/by/4.0/>), which permits unrestricted use, distribution, and reproduction in any medium, provided the original work is properly cited. The authors retain copyright of their work, and no permission is required from the authors or the publisher to reuse or distribute this article, as long as proper attribution is given to the original source.

1. Introduction

Unwanted water from several commercial sources, particularly the textile industry, poses significant environmental concerns [1,2]. Most organic dye molecules possess exceptional stability, which complicates their breakdown. When ingested through contaminated water, these dye molecules can be harmful to aquatic life, causing life-threatening diseases in animals. According to a survey by the World Health Organization (WHO), 2.2 million people perish because of contaminated water [3]. Compared to the conventional wastewater treatment approach, photocatalysis would be the most successful method to degrade organic dye molecules from wastewater [4]. Dye degradation can be carried out using various materials; cerium oxide holds a distinctive place among various nanomaterials due to its particular structure and thermal stability [5-7].

Metal-doped CeO₂ nanostructures can be produced in a number of ways, including the chemical vapor deposition method [8], microwave-assisted combustion method [9], solution combustion method [10], thermal decomposition method [11], sol-gel method [12], etc. Solution combustion synthesis is one of the comprehensible methods because it is distinguished

by a straightforward experimental setup, is associated with time and energy savings, and affords homogeneous end products [13-15].

The current work focuses on employing the *Lobularia maritima* plant seed extract as a fuel for the preparation of Zr-doped CeO₂ nanoparticles using a solution combustion method. The synthesized nanoparticle was then calcined to produce a uniform particle size. The synthesized nanoparticle was characterized by using a powder X-ray diffraction (PXRD), scanning electron microscopy (SEM), energy dispersive X-ray analysis (EDX), and Fourier transform infrared spectroscopy (FT-IR), and ultraviolet-visible diffuse reflectance spectroscopy (UV-DRS). Finally, it was also evaluated for the degradation of MB dye. The electrical behavior was also studied in this nanostructure. The frequency spectrum in this study shows a decreasing trend, whereas both the dielectric constant and dissipation factor were observed to be high at 10 Hz and 10 kHz, respectively. Advanced energy storage technologies, such as thin film capacitors, may benefit from the combination of improved electrical properties.

2. Materials and Methods

2.1. Materials.

The starting materials, including cerium nitrate hexahydrate (Ce(NO₃)₃ x 6H₂O) and Zirconyl nitrate hydrate (ZrO(NO₃)₂ x H₂O) were used in analytical grade acquired from Merck and were used without further purification.

2.2. Preparation of *Lobularia maritima* seed extract.

0.5 g of *Lobularia maritima* plant seeds were crushed and weighed, then transferred into a 100 ml beaker containing 20 ml of distilled water, and the mixture was warmed up to 40°C with proper stirring for 30 minutes. The mixture was filtered, and the filtrate was taken as a fuel for the synthesis of nanoparticles, as shown in Figure 1.

2.3. Preparation of Zr_{0.075}-Ce_{0.925}O₂ nanoparticle.

Cerium nitrate hexahydrate (99.99%) and Zirconyl nitrate hydrate (99.99%) were employed as precursors. Each of the nitrates was dissolved in distilled water separately, and the freshly prepared solutions containing 92.5 and 7.5 mol% of cerium nitrate hexahydrate and zirconyl nitrate hydrate, respectively, were mixed. To the above solution of nitrates, the plant seed extract was added, which serves as a fuel source. The mixture was stirred for 30 minutes to obtain a homogeneous solution. The combustion reaction was performed at 500°C for 5 hours in the combustion chamber. The yellow compound (Figure 1) was finally contained, and it was kept for calcination for about two hours at 500°C.



Figure 1. Plant seed extract and Zr_{0.075}-Ce_{0.925}O₂ nanoparticle.

3. Results and Discussion

3.1. X-ray diffraction analysis.

The formation of $\text{Zr}_{0.075}\text{-Ce}_{0.925}\text{-O}_2$ nanoparticle was confirmed by X-ray diffraction technique, as shown in Figure 2. According to the planes (111), (200), (220), (222), and (311), the corresponding peak positions are 28.4° , 33.09° , 47.2° , 56.2° , and 76.8° respectively. This indicates that the face-centered cubic (fcc) system is in accordance with the cubic fluorite structure (PDF file no. 34-0394) [16]. Further, the spectrum showed that the compound is pure and free from impurities, as depicted in Figure 2. The peak intensity of Zr-doped cerium oxide nanoparticles is less compared with that of CeO_2 nanoparticles. This finding demonstrates that with increasing the concentration of doping, the degree of sample crystallization gets reduced [17], which is clearly shown in Figure 2.

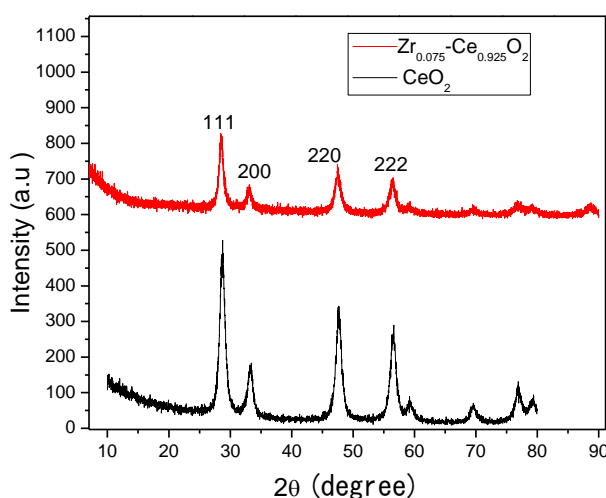


Figure 2. Powder XRD-Plot of $\text{Zr}_{0.075}\text{-Ce}_{0.925}\text{O}_2$ and CeO_2 nanoparticles.

3.2. SEM and EDX analysis.

The morphological features of $\text{Zr}_{0.075}\text{-Ce}_{0.925}\text{O}_2$ nanoparticles were examined using scanning electron microscopy (SEM) (Figure 3). Low-magnification micrographs of the prepared catalyst revealed that the catalyst was unevenly dispersed and had appreciably separated layers and flakelike structures with non-uniform thickness (Figure 3). The particulate arrangement was discovered to result in high porosity, characterized by widespread pore structures ranging from 10 nm to 50 nm. This porous nature of the material is attributed to its mesoporous characteristics. These micrographs clearly showed that the catalyst has high porosity and can provide a good channel for the catalytic processes. The ordered structure arises due to controlled experimental parameters followed during the preparation.

The elemental composition of the generated nanomaterial has been determined using energy-dispersive X-ray spectroscopy (EDX). The results indicated that the catalyst possesses all elements Ce, Zr, O, and trace amounts of N and C and appeared during its XPS processing (Figure 4); the EDX spectrum clearly shows the high-order purity of the nanoparticle with no additional impurity peaks. The stoichiometry calculated from the EDX mapping had a good correlation with the theoretical process.

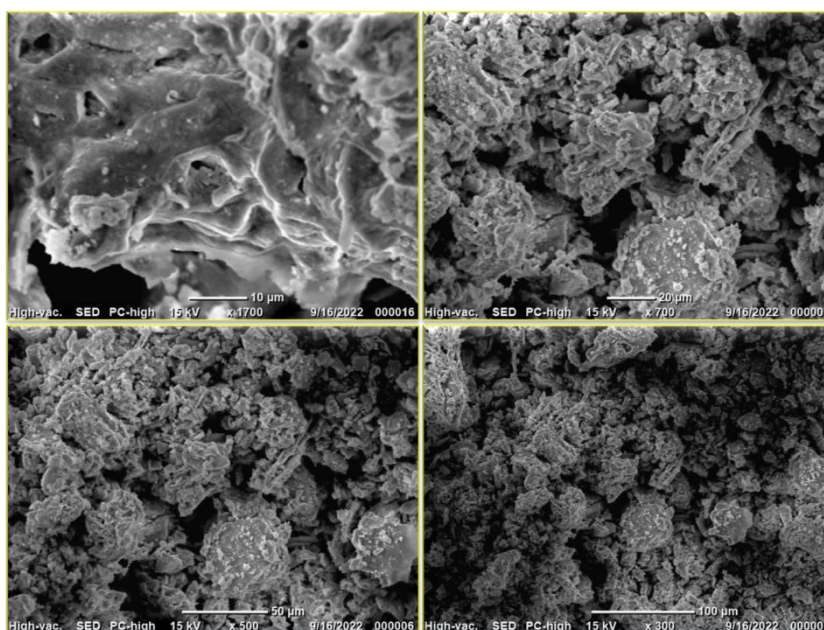


Figure 3. FESEM images of prepared Zr_{0.075}-Ce_{0.925}O₂ nanoparticles.

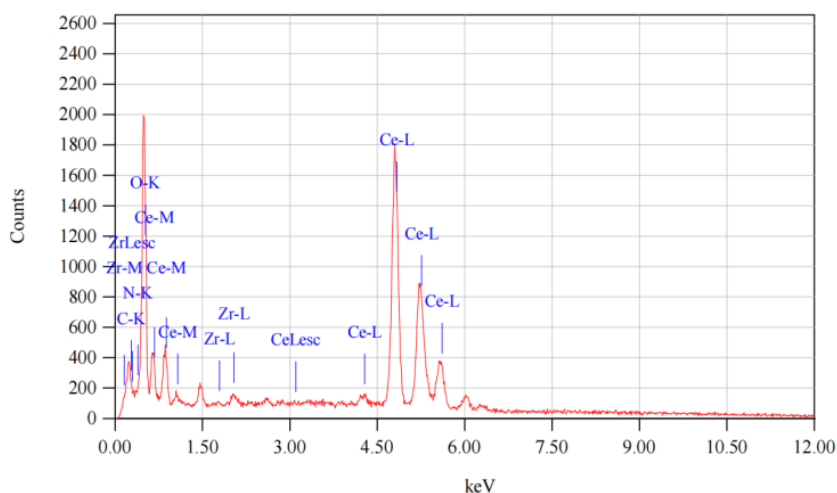


Figure 4. EDX analysis of prepared Zr_{0.075}-Ce_{0.925}O₂ nanoparticles.

3.3. FT-IR-based techniques.

The FT-IR spectrum of Zr_{0.075}-Ce_{0.925}O₂ nanoparticle was examined at room temperature in the wave number range of 400–4000 cm⁻¹. The peaks that appeared at 1621 cm⁻¹ and 1400 cm⁻¹ in the spectrum (Figure 5) are attributed to the symmetric and asymmetric stretching vibrations of the -C=O group, respectively. The peaks at 741 cm⁻¹ and 598 cm⁻¹ are attributed to the Ce-O bending vibrations and O-Ce-O stretching vibration modes, respectively [18], and were considered as the fingerprint support for the creation of Zr_{0.075}-Ce_{0.925}O₂ nanoparticle. Furthermore, a broad peak appears at the region of 3440 cm⁻¹, which is attributed to -OH stretching [19].

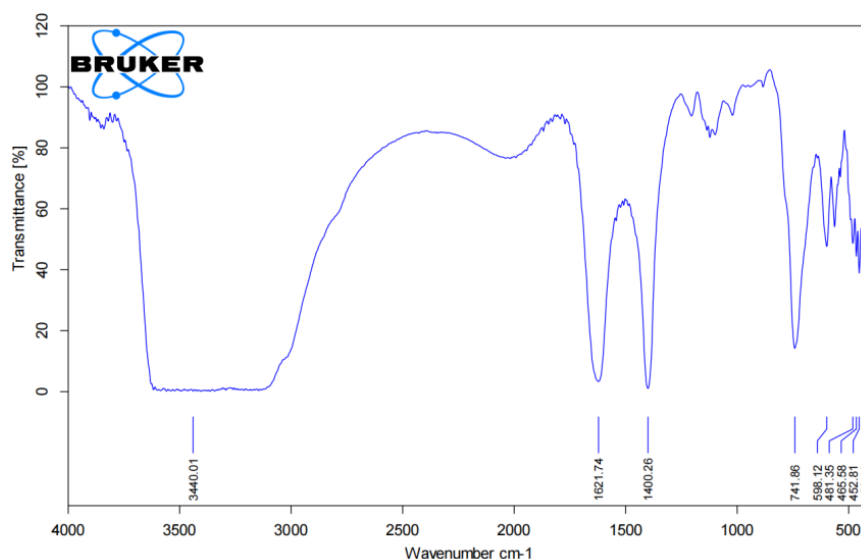


Figure 5. FT-IR spectrum of $Zr_{0.075}\text{-Ce}_{0.925}\text{O}_2$ nanoparticles.

3.4. Band gap analysis: UV-DRS analysis.

The synthesized nanoparticle was also subjected to UV-visible spectral analysis for their optical properties. According to a previous study, the band gap of pure CeO_2 is 3.4 eV [20]. In the current investigation, the band gap of $Zr_{0.075}\text{-Ce}_{0.925}\text{O}_2$ nanoparticle was found to be 2.9 eV, which proves that the produced catalysts are very effective visible light harnessing material. The usual Kubelka-Monk function was used to compute the catalyst's optical band energy (Figure 6a). The catalyst reflectance band was seen at 480 nm, as shown in Figure (6b).

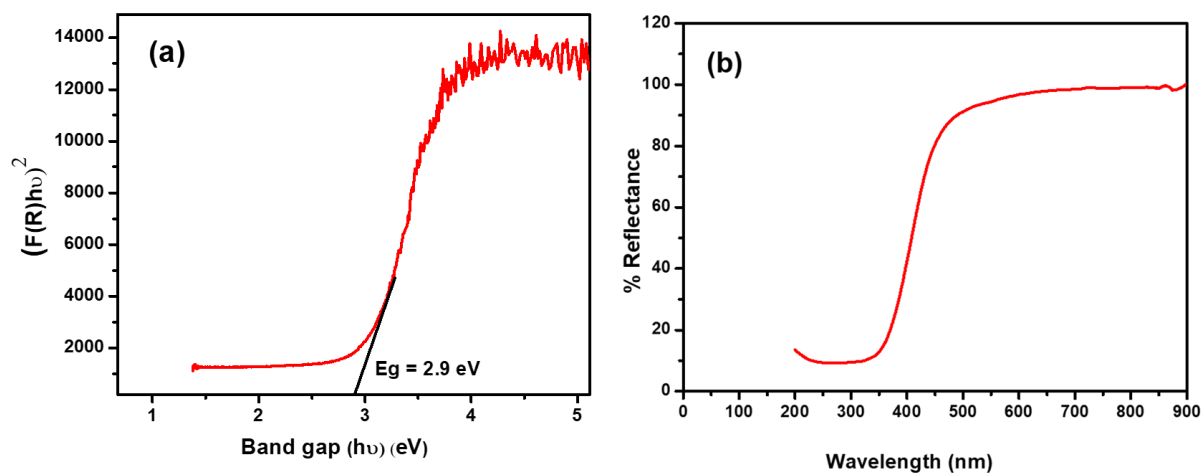


Figure 6. Optical bandgap (a) and reflectance; (b) plots of $Zr_{0.075}\text{-Ce}_{0.925}\text{O}_2$ nanoparticles.

3.4. Electrical properties.

The changes in the value of the dielectric constant (ϵ_r) of cerium-zirconium nanoparticles with frequency are indicated in Figure 7 (a). It was observed that the increase of frequency from 10 Hz to 8 MHz caused a decrease in the ϵ_r value. The highest value of ϵ_r (1360) was achieved at 10 Hz. There is a decreasing trend of ϵ_r observed with an increase in frequency. The higher dielectric constant (ϵ_r) at 10 Hz is because of the interfacial polarization process occurring because of a higher number of oxygen positions and the large aspect ratio of the nanofillers. When an electric field is applied to nanoparticles, charges located in the nanoparticles change their position and get stuck at different positions at the interfaces; thereby,

there is a formation of dipole moments. Maxwell-Wagner dielectric dispersion theory depicts and proves that the interfacial-polarization process occurs at lower frequencies and orientational-polarization at higher frequencies [21]. An electron finds it difficult to line up with the applied field, and thus, the polarization effect reduces, thus reducing ϵ_r [22]. Kumar et al. stated a similar trend in Lanthanum-added CeO₂ composites with a higher ϵ_r value of 120 [23].

The trend of the dissipation factor ($\tan \delta$) of Cerium-Zirconium nanoparticles with frequency is observed in Figure 7 (b). With an increase in frequency, the $\tan \delta$ value decreases. The highest value of the dissipation factor is observed at 10 kHz, which decreases with a further increase in frequency. Thus, the relaxation mechanism is the cause for these changes in the dissipation factor. The dissipation factor increases up to 10 kHz due to a frequency-dependent hopping process in the nanoparticles based on the charge carrier phenomenon [24].

The large storage capacity of capacitors requires both smaller dissipation factor values and higher dielectric constant values. As a result, the composite material used as the dielectric media directly affects the capacitor's dielectric constant. Further, $\tan \delta$ decreases with an increase in frequency. It is mainly attributed to drift in the dipole position with an applied electric field, which accounts for rapid alignment changes and causes heat loss. The dissipation factor values are reasonably trivial and ascribed to the low heat losses. A similar trend is reported in the literature [25].

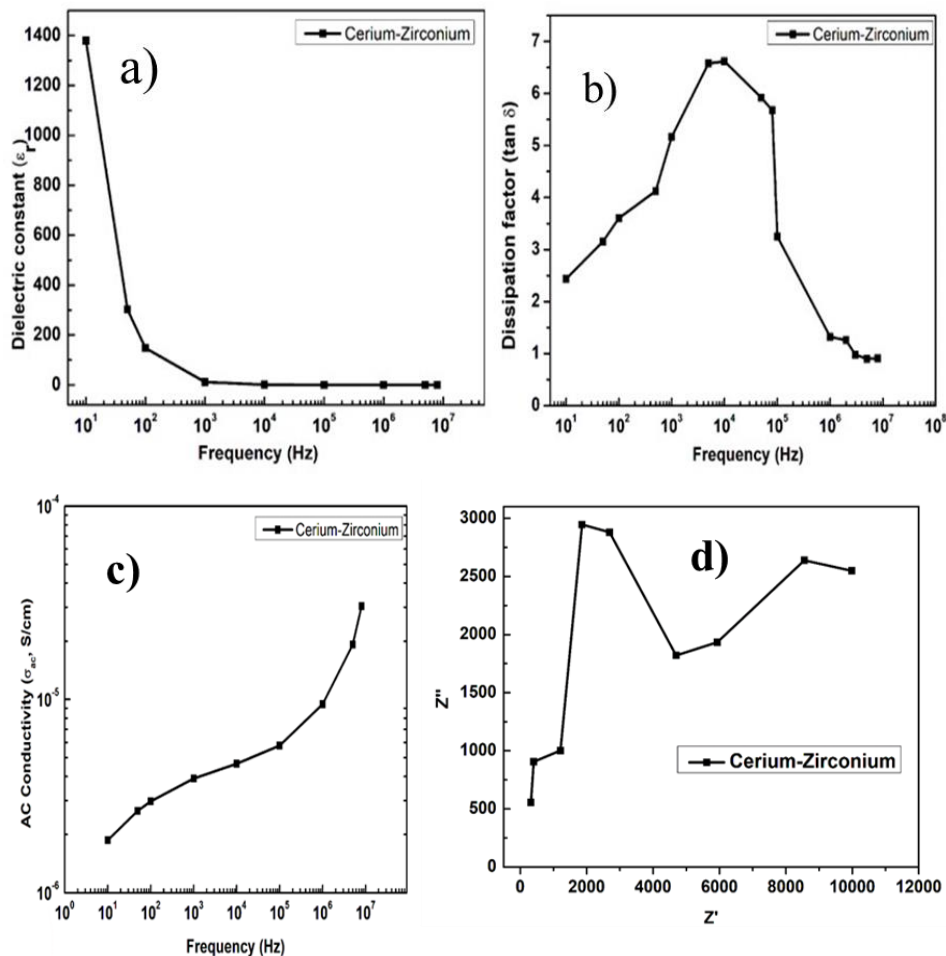


Figure 7. (a) Broadband dielectric constant (ϵ_r) characteristics with cerium-zirconium nanoparticles; (b) broadband dissipation factor ($\tan \delta$) with cerium-zirconium nanoparticles; (c) Broadband conductivity (σ_{ac}) of CERIUM-ZIRCONIUM nanoparticles; (d) Real and imaginary impedance plot (Cole-Cole plot) of Zr_{0.075}-Ce_{0.925}O₂ nanoparticles.

The variation in AC conductivity of cerium-zirconium nanoparticles with frequency is observed as depicted in Figure 7(c). An increase in frequency leads to a decrease in AC conductivity and is attributed to the electron-hopping mechanism. The movement of charge transporters is very important in the variation of AC conductivity of nanomaterials. Zr^{4+} ions replace Ce^{4+} ions in these structures, resulting in the development of polaron hopping with O^{2-} ions. This is more dominant at higher frequencies, which results in higher AC conductivity values. A similar trend is reported in the literature [26].

Figure 7(d) represents the Cole-Cole plot of Cerium-Zirconium nanoparticles. The complex impedance plot is analyzed to determine the influence of grain, grain boundary, and electrode interface effects on polarization. The polarization effect is represented by a semicircular curve. The characteristic feature of the semicircular curve represents the relaxation mechanism. The Cerium-Zirconium nanoparticles with grain homogeneity are characterized by an ideal Debye-type relaxation, represented by a semicircular curve with a center on the real Z' axis. The grain size of Cerium-Zirconium nanoparticles is not uniform [27,28]. The distribution of relaxation time is indicated by semicircles that grow depressed at higher frequencies and inclined towards the real axis of Z' axis [29].

3.5. Photocatalytic activity.

The process of measuring photocatalytic activity was executed by referring to prior research literature [30]. 100 mg of pure nanoparticles were added to 100 ml of a 5 ppm aqueous solution of methylene blue (MB) dye, and the complete setup was kept under visible light and constantly stirred. At 30-minute intervals, around 5 ml of solution was extracted from the reaction mixture, and the absorbance was measured. The absorbance gradually lowers over time (Figure 8a), demonstrating that Zr metal-doped CeO_2 is a better photocatalytic material. After 150 minutes, the percentage degradation rate of MB dye was found to be 82.6, as depicted in Figure 8b.

The percentage degradation of dye was estimated using the formula [31]:

$$\% D = \frac{C_0 - C}{C_0} \times 100 \quad (1)$$

Where C_0 and C are the initial and remaining concentrations of MB, respectively.

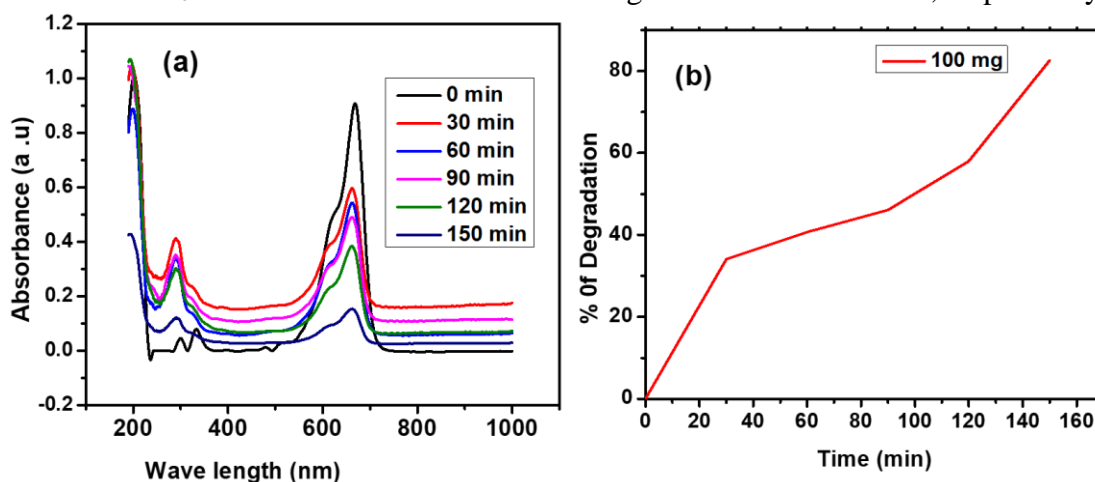


Figure 8. Plots of (a) UV-visible absorbance spectra showing the degradation of MB dye by $Zr_{0.075}-Ce_{0.925}O_2$ nanoparticle; (b) % of degradation with time.

4. Conclusions

The solution combustion technique was utilized to synthesize $Zr_{0.075}\text{-Ce}_{0.925}\text{O}_2$ nanoparticles. FESEM and XRD studies were used to study their structural and surface morphology. The UV-DRS tests revealed that the bandgap of nanoparticles is 2.90 eV, indicating that the produced catalyst is an effective visible light-harnessing material. The degradation of MB dye was examined using the photocatalytic activity of the generated nanoparticles. The plot indicates that it happens over time under visible light, and the percentage of degradation was determined to be 82.6 in 150 minutes. Using the LCR technique, the electrical characteristics of nanoparticles were investigated. The plot reveals that AC conductivity improves with frequency, and the dielectric constant decreases with frequency.

Author Contributions

All authors have read and agreed to the published version of the manuscript.

Institutional Review Board Statement

Not applicable.

Informed Consent Statement

Not applicable.

Data Availability Statement

Data supporting the findings of this study are available upon reasonable request from the corresponding author.

Funding

This research received no external funding.

Acknowledgments

The authors are thankful to the Siddaganga Institute of Technology and Department of Studies and Research in Chemistry, Tumkur University, Tumakuru, for providing the laboratory facility to carry out this work.

Conflicts of Interest

The authors declare no conflict of interest.

Reference

1. Manganyi, M.C.; Dikobe, T.B.; Maseme, M.R. Exploring the Potential of Endophytic Microorganisms and Nanoparticles for Enhanced Water Remediation. *Molecules* **2024**, *29*, 2858, <https://doi.org/10.3390/molecules29122858>.
2. Khan, W.U.; Ahmed, S.; Dhoble, Y.; Madhav, S. A critical review of hazardous waste generation from textile industries and associated ecological impacts. *J. Indian Chem. Soc.* **2023**, *100*, 100829, <https://doi.org/10.1016/j.jics.2022.100829>.

3. Saleh, R.; Djaja, N.F. Transition-metal-doped ZnO nanoparticles: Synthesis, characterization and photocatalytic activity under UV light. *Spectrochim. Acta - A: Mol. Biomol. Spectrosc.* **2014**, *130*, 581-590, <https://doi.org/10.1016/j.saa.2014.03.089>.
4. Alex, J.; Rajkumar, S.; PrincyMerlin, J.; Aravind, A.; Sajan, D.; Praveen, C.S. Single step auto-igniting combustion technique grown CeO₂ and Ni-doped CeO₂ nanostructures for multifunctional applications. *J. Alloys Compd.* **2021**, *882*, 160409, <https://doi.org/10.1016/j.jallcom.2021.160409>.
5. Mishra, S.; Sundaram, B. A review of the photocatalysis process used for wastewater treatment. *Mater. Today:Proc.* **2024**, *102*, 393-409, <https://doi.org/10.1016/j.matpr.2023.07.147>.
6. Gallucci, N.; Hmoudah, M.; Martinez, E.; El-Qanni, A.; Di Serio, M.; Paduano, L.; Vitiello, G.; Russo, V. Photodegradation of ibuprofen using CeO₂ nanostructured materials: Reaction kinetics, modeling, and thermodynamics. *J. Environ. Chem. Eng.* **2022**, *10*, 107866, <https://doi.org/10.1016/j.jece.2022.107866>.
7. Pathak, V.; Lad, P.; Thakkar, A.B.; Thakor, P.; Deshpande, M.P.; Pandya, S. Synthesis, characterization and applications of cubic fluorite cerium oxide nanoparticles: A comprehensive study. *Res. Surf. Interfaces* **2023**, *11*, 100111, <https://doi.org/10.1016/j.rsurfi.2023.100111>.
8. Fu, J.; Sun, Y.; Ji, Y.; Zhang, J. Fabrication of robust ceramic based superhydrophobic coating on aluminum substrate via plasma electrolytic oxidation and chemical vapor deposition methods. *J. Mater. Process. Technol.* **2022**, *306*, 117641, <https://doi.org/10.1016/j.jmatprotec.2022.117641>.
9. Lakshmanan, A.; Surendran, P.; Sakthy Priya, S.; Balakrishnan, K.; Rameshkumar, P.; Kannan, K.; Mahalakshmi, K.; Gayathri, V.; Vinitha, G. Investigations on structural, dielectric, and third-order nonlinear optical studies of Ni_{0.5}Zn_{0.5}Fe₂O₄ nanoparticles by microwave combustion method with different fuels (glycine, urea and citric acid). *Mater. Lett.* **2024**, *360*, 135973, <https://doi.org/10.1016/j.matlet.2024.135973>.
10. Khyrun, S.M.F.; Christy, A.J.; Usha, R.; Nehru, L.C.; Suresh, S. Novel solution combustion synthesis of CeO₂/CuO nanocomposite for photocatalytic and biological applications. *Opt. Mater.* **2023**, *139*, 113756, <https://doi.org/10.1016/j.optmat.2023.113756>.
11. Tan, L.; Xu, J.; Zhang, X.; Hang, Z.; Jia, Y.; Wang, S. Synthesis of g-C₃N₄/CeO₂ nanocomposites with improved catalytic activity on the thermal decomposition of ammonium perchlorate. *Appl. Surf. Sci.* **2015**, *356*, 447-453, <https://doi.org/10.1016/j.apsusc.2015.08.078>.
12. Yang, H.; Zhu, M.; Li, Y. Sol-gel research in China: a brief history and recent research trends in synthesis of sol-gel derived materials and their applications. *J Sol-Gel Sci. Technol.* **2023**, *106*, 406-421, <https://doi.org/10.1007/s10971-022-05750-y>.
13. Karthik, A.S.; Agrawal, S.; Senthil, S. One-pot synthesis of g-C₃N₄/N-doped CeO₂ nanocomposites and their potential visible light-driven photocatalytic degradation of methylene blue dye. *Environ Geochem Health* **2024**, *246*, <https://doi.org/10.1007/s10653-024-02007-1>.
14. Naidi, S.N.; Khan, F.; Harunsani, M.H.; Tan, A.L.; Kim, Y.-M.; Khan, M.M. Effect of Zr doping on photoantioxidant and antibiofilm properties of CeO₂ NPs fabricated using aqueous leaf extract of *Pometia pinnata*. *Bioprocess Biosyst. Eng.* **2022**, *45*, 279-295, <https://doi.org/10.1007/s00449-021-02656-x>.
15. Siddique, F.; Gonzalez-Cortes, S.; Mirzaei, A.; Xiao, T.; Rafiq, M.A.; Zhang, X. Solution combustion synthesis: the relevant metrics for producing advanced and nanostructured photocatalysts. *Nanoscale* **2022**, *14*, 11806-11868, <https://doi.org/10.1039/D2NR02714C>.
16. Shang, Z.; Yu, Y.; Yang, H.; Yang, Z.; Xiao, Y.; Wang, X. One-step solution combustion synthesis of micro-nano-scale porous Cu/CeO₂ with enhanced photocatalytic properties. *J. Rare Earths* **2023**, *41*, 250-258, <https://doi.org/10.1016/j.jre.2022.02.013>.
17. Luo, N.; Fan, L.; Chen, Y.; Lan, W. Construction of Oxygen Vacancies of Zr-Doped CeO₂ with Enhanced Dye Adsorption Performance. *Crystals* **2023**, *13*, 1641, <https://doi.org/10.3390/cryst13121641>.
18. Naidi, S.N.; Khan, F.; Tan, A.L.; Harunsani, M.H.; Kim, Y.-M.; Khan, M.M. Green synthesis of CeO₂ and Zr/Sn-dual doped CeO₂ nanoparticles with photoantioxidant and antibiofilm activities. *Biomater. Sci.* **2021**, *9*, 4854-4869, <https://doi.org/10.1039/D1BM00298H>.
19. Iqbal, A.; Obaidurrahman, M.; Ahmed, A.S.; Choi, B.-S.; Ahmed, A. Influence of Gd³⁺ ions on structural, optical and magnetic properties of CeO₂ nanoparticles: a comprehensive study. *Appl. Phys. A* **2023**, *129*, 80, <https://doi.org/10.1007/s00339-022-06371-6>.
20. Ali, S.R.; Kumar, R.; Kalam, A.; Al-Sehemi, A.G.; Arya, M.C. Effect of Strontium Doping on the Band Gap of CeO₂ Nanoparticles Synthesized Using Facile Co-precipitation. *Arab. J. Sci. Eng.* **2019**, *44*, 6295-6302, <https://doi.org/10.1007/s13369-018-03700-x>.

21. Desmond, M.; Mavrogiannis, N.; Gagnon, Z. Maxwell-Wagner Polarization and Frequency-Dependent Injection at Aqueous Electrical Interfaces. *Phys. Rev. Lett.* **2012**, *109*, 187602, <https://doi.org/10.1103/PhysRevLett.109.187602>.
22. Abbas, S.K.; Atiq, S.; Riaz, S.; Ramay, S.M.; Naseem, S. Thermally assisted electro-active regions in SrMnO₃ ceramics. *Mater. Chem. Phys.* **2017**, *200*, 128-135, <https://doi.org/10.1016/j.matchemphys.2017.07.039>.
23. Kishor Kumar, M.J.; Kalathi, J.T. Low-temperature sonochemical synthesis of high dielectric Lanthanum doped Cerium oxide nanopowder. *J. Alloys Compd.* **2018**, *748*, 348-354, <https://doi.org/10.1016/j.jallcom.2018.03.096>.
24. Kumar, U.; Upadhyay, S. Studies on dielectric and electrical properties of Ruddlesden-Popper oxide Sr₂SnO₄. *Mater. Lett.* **2018**, *227*, 100-103, <https://doi.org/10.1016/j.matlet.2018.05.046>.
25. Abbas, S.K.; Aslam, M.A.; Amir, M.; Atiq, S.; Ahmed, Z.; Siddiqi, S.A.; Naseem, S. Electrical impedance functionality and spin orientation transformation of nanostructured Sr-substituted BaMnO₃ hexagonal perovskites. *J. Alloys Compd.* **2017**, *712*, 720-731, <https://doi.org/10.1016/j.jallcom.2017.04.161>.
26. Cole, K.S.; Cole, R.H. Dispersion and Absorption in Dielectrics I. Alternating Current Characteristics. *J. Chem. Phys.* **1941**, *9*, 341-351, <https://doi.org/10.1063/1.1750906>.
27. Garbarz-Glos, B.; Bąk, W.; Antonova, M.; Pawlik, M. Structural, microstructural and impedance spectroscopy study of functional ferroelectric ceramic materials based on barium titanate. *OP Conf. Ser.: Mater. Sci. Eng.* **2013**, *49*, 012031, <https://doi.org/10.1088/1757-899X/49/1/012031>.
28. Sahoo, S.; Mahapatra, P.K.; Choudhary, R.N.P.; Alagarsamy, P. Influence of compositional variation on structural, electrical and magnetic characteristics of (Ba_{1-x}Gd) (Ti_{1-x}Fex) O₃ (0.2 ≤ x ≤ 0.5). *Mater. Res. Express* **2018**, *5*, 016101, <https://doi.org/10.1088/2053-1591/aa9efb>.
29. Gupta, P.; Padhee, R.; Mahapatra, P.K.; Choudhary, R.N.P.; Das, S. Structural and electrical properties of Bi₃TiVO₉ ferroelectric ceramics. *J. Alloys Compd.* **2018**, *731*, 1171-1180, <https://doi.org/10.1016/j.jallcom.2017.10.123>.
30. Nethravathi, P.C.; Suresh, D. Silver-doped ZnO embedded reduced graphene oxide hybrid nanostructured composites for superior photocatalytic hydrogen generation, dye degradation, nitrite sensing and antioxidant activities. *Inorg. Chem. Commun.* **2021**, *134*, 109051, <https://doi.org/10.1016/j.inoche.2021.109051>.
31. Khan, S.; Noor, A.; Khan, I.; Muhammad, M.; Sadiq, M.; Muhammad, N. Photocatalytic Degradation of Organic Dyes Contaminated Aqueous Solution Using Binary CdTiO₂ and Ternary NiCdTiO₂ Nanocomposites. *Catalysts* **2023**, *13*, 44, <https://doi.org/10.3390/catal13010044>.

Publisher's Note & Disclaimer

The statements, opinions, and data presented in this publication are solely those of the individual author(s) and contributor(s) and do not necessarily reflect the views of the publisher and/or the editor(s). The publisher and/or the editor(s) disclaim any responsibility for the accuracy, completeness, or reliability of the content. Neither the publisher nor the editor(s) assume any legal liability for any errors, omissions, or consequences arising from the use of the information presented in this publication. Furthermore, the publisher and/or the editor(s) disclaim any liability for any injury, damage, or loss to persons or property that may result from the use of any ideas, methods, instructions, or products mentioned in the content. Readers are encouraged to independently verify any information before relying on it, and the publisher assumes no responsibility for any consequences arising from the use of materials contained in this publication.